Proceedings of the ASME 2021 Virtual International Design Engineering Technical Conferences & Computers and Information in Engineering Conference
IDETC-CIE 2021
Virtual Conference: August 17 – 20, 2021

DETC2021-69028

NONLINEAR ANALYSIS OF A CLASS OF INVERSION-BASED COMPLIANT CROSS-SPRING PIVOTS

Shiyao Li[1], Guangbo Hao[1,*], Yingyue Chen[1], Jiaxiang Zhu[1], Giovanni Berselli[2]

[1]School of Engineering and Architecture, University College Cork, Cork, Ireland
[2]Department of Mechanical, Energy, Management and Transportation Engineering, University of Genova, Genova, Italy
*Corresponding author. E-mail address: G.Hao@ucc.ie (G. Hao)

ABSTRACT

This paper presents a nonlinear model of an inversion-based generalized cross-spring pivot (IG-CSP) using the beam constraint model (BCM), which can be employed for the geometric error analysis and the characteristic analysis of an inversion-based symmetric cross-spring pivot (IS-CSP). The load-dependent effects are classified in two ways, including structure load-dependent effects and beam load-dependent effects, where the loading positions, geometric parameters of elastic flexures, and axial forces are the main contributing factors. The closed-form load-rotation relations of an IS-CSP and a non-inversion-based symmetric cross-spring pivot (NIS-CSP) are derived with consideration of the three contributing factors for analyzing the load-dependent effects. The load-dependent effects of IS-CSP and NIS-CSP are compared when the loading position is fixed. The rotational stiffness of the IS-CSP or NIS-CSP can be designed to increase, decrease, or remain constant with axial forces, by regulating the balance between the loading positions and the geometric parameters. The closed-form solution of the center shift of an IS-CSP is derived. The effects of axial forces on the IS-CSP center shift are analyzed and compared with those of a NIS-CSP. Finally, based on the nonlinear analysis results of IS-CSP and NIS-CSP, two new compound symmetric cross-spring pivots are presented and analyzed via analytical and FEA models.

Keywords: Compliant cross-spring pivot; load-dependent effects; loading positions; center shift; nonlinear analysis

1. INTRODUCTION

A compliant generalized cross-spring pivot (G-CSP) consists of two flexure sheets, including the symmetric cross-spring pivot (S-CSP) [1]–[4] and the asymmetric cross-spring pivot. It can provide rotational motions with its rotational center at the intersection of the two flexure sheets. We classify the G-CSP as shown in Fig. 1.

The S-CSP is our focus in this paper, which has been widely studied[5]–[8], including the non-inversion-based (traditional) symmetric cross-spring pivot (NIS-CSP) and the inversion-based cross-spring pivot (IS-CSP). The beam constraint model (BCM) [9]–[11], pseudo-rigid-body model (PRBM) [2,12], numerical approaches [13], and finite element analysis (FEA) are commonly used for modelling nonlinearities of such compliant mechanisms. The BCM is accurate enough when the deflection of an elastic flexure is in an intermediate range. A number of closed-form models of compliant mechanisms based on the BCM have been derived for quickly analyzing parameters and for providing design insights, such as the work by Hao et al.[14] and Zhao et al.[9]. In this paper, our analysis is based on the BCM and FEA verification. We derive the nonlinear analytical model of an inversion-based generalized cross-spring pivot (IG-CSP). This model can be used for the geometrical error analysis of the IS-CSP due to machining imperfections, and the nonlinear analytical model of an IS-CSP can be derived quickly. This is the first motivation of our paper.

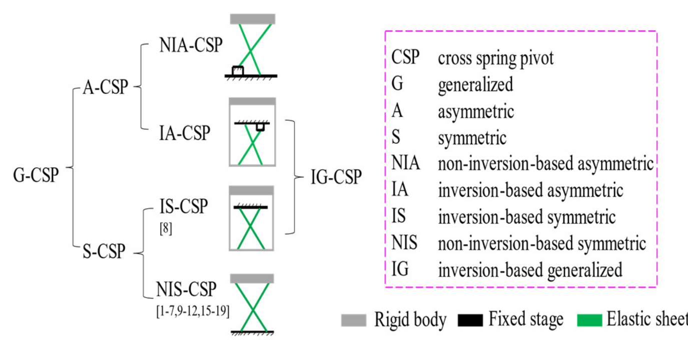

FIGURE 1: The categories of the generalized cross-spring pivot.

Axial loads can lead to strong nonlinearities of the compliant mechanisms, motivating Zhao et al., along with other researchers, to have further analyzed the load-dependent effects of the NIS-CSP. Also the effects of the geometric parameters and bearing-direction loads on the rotational stiffness have been detailed in Refs.[15]–[19]. However, the loading position of bearing-direction loads is another important factor contributing to the load-dependent effects, and there are no reported papers investigating the loading-position effects on the rotational stiffness of the S-CSP, which is the second motivation of our work.

In this paper, load-dependent effects are divided into two categories, namely: 1) structure load-dependent; and 2) beam load-dependent effects. Here, the loading positions, geometric parameters of the sheets, and axial forces are three main contributing factors to such load-dependent effects, indicatively explained in Fig. 2.

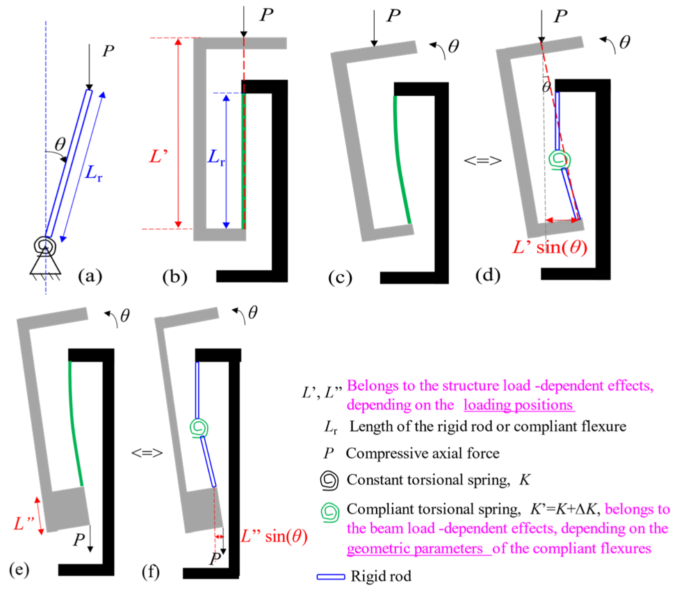

FIGURE 2: Load-dependent effects: (a) a compressive load (P) acting on the rigid rod; (b) a compressive load (P) acting on an inversed compliant mechanism;(c) the inversed compliant mechanism rotating at a small angle with P on the top of the motion stage; (d) demonstrating the equivalent stiffness K_{eff} of Fig. 2(c); (e) P acting at the bottom of the motion stage; and (f) demonstrating the equivalent stiffness K_{eff} of Fig.2(e)

The structure load-dependent effects can be explained as follows. In Fig. 2(a), a rigid rod connects with a constant torsional spring (stiffness denoted by K) on the ground, and a compressive axial force (denoted by P) acts on the free end of the rod. If the rod tilts, the effective rotational stiffness of the mechanism (denoted by K_{eff}) can be expressed as $K_{\text{eff}} = K - PL_r$ under a small angle assumption. K_{eff} decreases with the increase of P and L_r (the rod length). The beam load-dependent effects can be explained as follows. Let ΔK denote the rotational stiffness error correction term due to the beam load-dependent effects, whose absolute value depends on the geometric parameters of the flexure. When a tensile axial force acts on the free end of an elastic beam, the resulting rotational stiffness of the beam (i.e. $K'=K+\Delta K$) increases with the increase of the tensile axial force, i.e., $\Delta K>0$; When a compressive axial force acts on the free end, K' decrease with the increase of the compressive axial force, i.e. $\Delta K<0$ [20].

K_{eff} of the inversed compliant mechanism is a collective result of the structure and beam load-dependent effects. L' (or L'') and K' contribute to the structure and beam load-dependent effects, respectively. In Figs. 2(b) to (d), when P acts at the top of the motion stage of an inversed compliant mechanism, the effective rotational stiffness can be expressed as $K_{\text{eff}} = K' - PL'$ $=(K+\Delta K) - PL'$ under a small angle assumption. When $\Delta K>PL'$, K_{eff} increases with the axial loads; when $\Delta K = PL'$, K_{eff} keeps constant with the axial loads; when $\Delta K < PL'$, K_{eff} decreases with the axial load. When a compressive force acts on the top of the inversed compliant mechanism, K_{eff} can increase, decrease, or be constant. Similarly, in Figs. 2(e) and (f), if P acts at the bottom of the motion stage, $K_{\text{eff}} = K' + PL'' = (K+\Delta K) + PL''$ under a small angle assumption, which means K_{eff} can only increase with a compressive axial force. The equilibrium between structure and beam load-dependent effects of the inversed compliant mechanism is important for the stiffness control, which is the third motivation of our paper.

K_{eff} decreasing to quasi-zero [21] (i.e., first-order buckling in the rotation direction) should be avoided in a compliant mechanism. When a compressive axial/bearing-direction force acts on the NIS-CSP, the rotational stiffness can increase, decrease, or be constant, which relates to its geometric parameters and the axial forces [15], but the possibility of increasing rotational stiffness is relatively low. However, when a compressive axial force acts on the IS-CSP, the possibility of increasing rotational stiffness rises, thus leading to a higher possibility of avoiding buckling, which is the fourth motivation of our paper. Therefore, by combining the NIS-CSP and IS-CSP in a parallel arrangement, we propose a novel compound S-CSP whose rotational stiffness being insensitive to the axial load (i.e. no first-order buckling), which is robust to second-order buckling in the bearing direction.

Zhao et al. [9] derived the closed-form center shift model of a NIS-CSP and designed several novel compound NIS-CSPs to reduce the center shift. They analyzed the effects of geometric parameters on the center shift and obtained the parameters combination that can produce the smallest possible shift. The effects of the axial forces on the center shift of the NIS-CSP with these special parameters are detailed in Ref. [9]. Bi et al. [17] also analyzed axial load effects of a cartwheel flexure pivot. It is worth analyzing the effects of the axial forces on the S-CSP center shift with general parameters and comparatively evaluate center shifts of NIS-CSP and IS-CSP. This is the inspiration of another novel compound S-CSP with the NIS-CSP and IS-CSP arranged in series, whose center shift is minimized significantly.

We briefly summarize these motivations as follows.

(1) The nonlinear analytical or closed-form models of an IG-CSP based on BCM have not been reported. The nonlinear models are greatly needed for analyzing the geometrical errors and quickly deriving the analytical models of an IS-CSP. For instance, such relations may be used to optimize devices such as the knee rehabilitation oriented joint presented in [22].

(2) There is lack of investigations concerning the rotational stiffness of S-CSPs with respect to different loading positions.

(3) Problems concerning the equilibrium between structure and beam load-dependent effects, which controls the stiffness of an inversed compliant mechanism, shall be further analyzed.

(4) The analysis of loading-dependent effects and center shift of the IS-CSP and the NIS-CSP inspires us to propose two new compound S-CSPs with improved performances.

This paper is organized as below. Section 2 derives the nonlinear analytical model of the IG-CSP based on BCM, which can reduce to the closed-form model of the S-CSP. In Section 3, the load-rotation relation of an IS-CSP is derived, and the effects of the loading positions, geometric parametric, and the axial forces on the rotational stiffness are analyzed. The equilibrium between structure and beam load-dependent effects of the IS-CSP are analyzed for rotational stiffness regulation. The load-dependent effects of an IS-CSP and a NIS-CSP are compared. The closed-form center shift of an IS-CSP is derived, and the effects of the axial forces on the center shift of the IS-CSP are analyzed, which are also compared with those of a NIS-CSP. Section 4 presents two new compound S-CSPs, and each design consists of an IS-CSP and a NIS-CSP: design I is a parallel mechanism whereas design II is a serial mechanism. The conclusions are drawn in Section 5.

2. THE NONLINEAR ANALYSIS OF AN IG-CSP WITH TWO SHEETS

In this section, the normalization-based analytical model of an IG-CSP is derived, followed by a closed-form load-rotation relation of the IG-CSP under a small angle assumption. The IG-CSP can be modelled as two flexure sheets connected in a parallel arrangement. In line with Ref. [9], the analytical center-shift model of the IG-CSP is derived. The right-handed coordinate system and right-handed rule are used throughout this paper.

2.1 Normalization-based analytical model

The normalized analytical model of an IG-CSP is derived as below. The two sheets in the IG-CSP are numbered as, sheet 1 and sheet 2, respectively. The local coordinate systems of the two sheets are denoted as o_1-$x_1y_1z_1$ and o_2-$x_2y_2z_2$ with their origins locating at their free ends. L_i, T_i, and U_i denote the length, thickness, and width of sheet i (i = 1 or 2) along the x_i, y_i, and z_i-axes, respectively. U_1=U_2 and T_1=T_2 are required throughout this paper. External actual loads: F_{xi}, F_{yi}, and M_{zi} act at the origin, o_i. F_{xi} and F_{yi} denote pure forces along the x_i and y_i axes, respectively; M_{zi} denotes the pure moment about the z_i-axis. Sheet 1 with a local coordinate system o_1-$x_1y_1z_1$ is shown in Fig. 3.

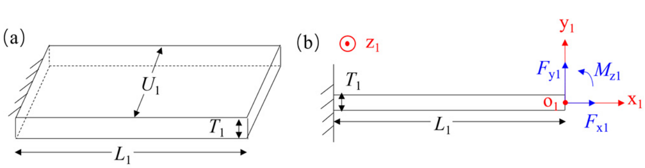

FIGURE 3: The definitions of sheet 1: (a) the sheet geometry, and (b) the local coordinate system and loads acting at the free end.

All translational displacements and length parameters are divided by L_1 (we assume that L_1 is longer than L_2 of the IG-CSP). Forces and moments are divided by EI_{z1}/L_1^2 and EI_{z1}/L_1, respectively [23], where I_{z1} denotes the cross-section moment of inertia about the z_1-axis and can be expressed as $U_1T_1^3/12$, and E is Young's Modulus of the material. Therefore, for sheet i (i=1 or 2), we use f_{xi} and f_{yi} to denote normalized forces, m_{zi} to denote normalized moments, d_{xi} and d_{yi} to denote normalized displacements; θ_{zi} to denote a rotational angle. The analytical models of the two sheets are shown in Eqs. (1) - (2) based on the BCM in [20].

$$d_{xi} = \frac{r_i f_{xi}}{d} + r_i \begin{bmatrix} \frac{d_{yi}}{r_i} & \theta_{zi} \end{bmatrix} \begin{bmatrix} -3/5 & 1/20 \\ 1/20 & -1/15 \end{bmatrix} \begin{bmatrix} \frac{d_{yi}}{r_i} \\ \theta_{zi} \end{bmatrix} + r_i^3 f_{xi} \begin{bmatrix} \frac{d_{yi}}{r_i} & \theta_{zi} \end{bmatrix} \begin{bmatrix} 1/700 & -1/1400 \\ -1/1400 & 11/6300 \end{bmatrix} \begin{bmatrix} \frac{d_{yi}}{r_i} \\ \theta_{zi} \end{bmatrix} \tag{1}$$

$$\begin{bmatrix} r_i^2 f_{yi} \\ r_i m_{zi} \end{bmatrix} = \begin{bmatrix} 12 & -6 \\ -6 & 4 \end{bmatrix} \begin{bmatrix} \frac{d_{yi}}{r_i} \\ \theta_{zi} \end{bmatrix} + r_i^2 f_{xi} \begin{bmatrix} 6/5 & -1/10 \\ -1/10 & 2/15 \end{bmatrix} \begin{bmatrix} \frac{d_{yi}}{r_i} \\ \theta_{zi} \end{bmatrix} \tag{2}$$

where, d=12/(T/L_1)^2; i=1 or 2, and r_1=1; r_2=L_2/L_1.

The IG-CSP is described in Fig. 4. O-XYZ denotes the global coordinate system of the IG-CSP, which locates at the motion stage with the Y-axis passing through the rotation center in the non-deformed configuration. The independent normalized parameters to define the IG-CSP include r_2, α_1, α_2, λ_1, and $\boldsymbol{h}$. The first four ones are independent geometric parameters, and the last one $\boldsymbol{h}$ is a vertical vector pointing from the free end of the sheet to the loading position. The absolute value of $\boldsymbol{h}$ is denoted by h, which relates to the loading position. h is equal to H/L_1, where H denotes the vertical distance between the free end of the sheet and the loading position. If $\boldsymbol{h}$ follows the direction of the Y-axis, h replaces $\boldsymbol{h}$ in the equations of this paper; otherwise,− h replaces $\boldsymbol{h}$. λ_2 can be derived from the equation $\lambda_1\cos(\alpha_1) = \lambda_2 r_2\cos(\alpha_2)$. We use f_{xs}, f_{ys}, and m_{zs} to denote the normalized loads of the IG-CSP acting at the origin, O, and use d_{xs}, d_{ys}, and θ_{zs} to denote the normalized displacements and rotational angle of the IG-CSP's motion stage (at point O).

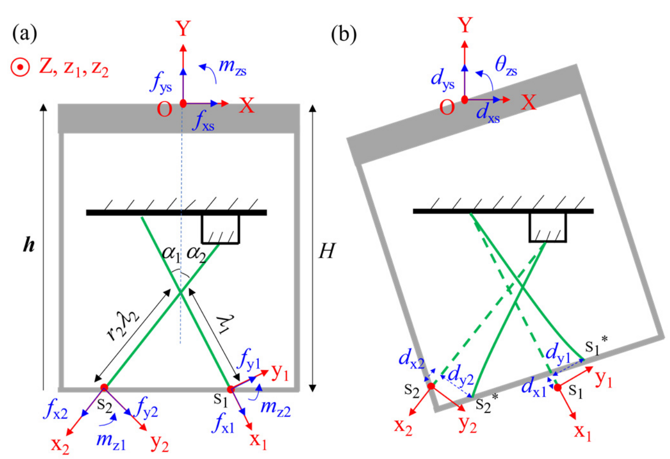

FIGURE 4: The description of the IG-CSP: (a) normalized geometric parameters and loads, and (b) the normalized displacements.

The compatibility conditions can be described as Eqs. (3) and (4) (derivation details can be seen in Ref. [14]).

$$[d_{x1}, d_{y1}, \theta_{z1}]^T = \mathbf{R}_{z1}(\mathbf{R}_{z3}\mathbf{S}_1 - \mathbf{S}_1) + [d_{xs}, d_{ys}, \theta_{zs}]^T \tag{3}$$

$$[d_{x2}, d_{y2}, \theta_{z2}]^T = \mathbf{R}_{z2}(\mathbf{R}_{z4}\mathbf{S}_2 - \mathbf{S}_2) + [d_{xs}, d_{ys}, \theta_{zs}]^T \tag{4}$$

where, $\mathbf{S}_1$ and $\mathbf{S}_2$ denote the coordinates of the points S_1, S_2 (Fig. 4) with regard to the global coordinate system, and are represented as follows. $\mathbf{S}_1=[\lambda_1\sin(\alpha_1), -\boldsymbol{h}, 0]^T$, $\mathbf{S}_2=[-\lambda_2 r_2\sin(\alpha_2), -\boldsymbol{h}, 0]^T$. $\mathbf{R}_{zj}$ (j=1, 2, 3 or 4) is a rotational matrix about the Z-axis, which is designated as $\mathbf{R}_{z1} = \begin{bmatrix} \cos\beta_j & -\sin\beta_j & 0 \\ \sin\beta_j & \cos\beta_j & 0 \\ 0 & 0 & 1 \end{bmatrix}$. $\beta_1=\pi/2-\alpha_1$, $\beta_2=\pi/2+\alpha_2$, $\beta_3=\theta_{z1}$, and $\beta_4=\theta_{z2}$.

The load-equilibrium conditions of the motion stage in the deformed configuration can be expressed Eq. (5) (See details in [14]).

$$[f_{xs}, f_{ys}, m_{zs}]^T = \mathbf{D}_{p1}^T\mathbf{R}_{z1}^T[f_{x1}, f_{y1}, m_{z1}]^T + \mathbf{D}_{p2}^T\mathbf{R}_{z2}^T[f_{x2}, f_{y2}, m_{z2}]^T \tag{5}$$

where, $\mathbf{D}_{pi}$ (i=1 or 2) denotes a translational matrix, $\mathbf{D}_{pi}^T = \begin{bmatrix} 1 & 0 & -\mathbf{S}_i^*(2,1) \\ 0 & 1 & \mathbf{S}_i^*(1,1) \\ 0 & 0 & 1 \end{bmatrix}$. $\mathbf{S}_i^*$ (i=1 or 2) denotes the coordinates of the point S_i relative to the global coordinate system after only the rotation of the motion stage, and $\mathbf{S}_i^*=\mathbf{R}_{zs}\mathbf{S}_i$. $\mathbf{R}_{zs}$ is a rotational matrix about the Z-axis, $\mathbf{R}_{zs} = \begin{bmatrix} \cos(\theta_{zs}) & -\sin(\theta_{zs}) & 0 \\ \sin(\theta_{zs}) & \cos(\theta_{zs}) & 0 \\ 0 & 0 & 1 \end{bmatrix}$.

Given the independent parameters and three loading inputs (f_{xs}, f_{ys}, and m_{zs}), the outputs of the motion stage (d_{xs}, d_{ys} and θ_{zs}) are solved by the Eqs. (1) through (5). These solutions refer to analytical models in this paper.

In order to derive the closed-form rotations (Eq. (7)) of the IG-CSP, we use Eq. (6) to simplify the results of d_{y1} and d_{y2} [9], [17], and use small-angle approximations to derive the closed-form rotational angle of the IG-CSP (Eq. (7)). The small-angle approximations are based on $\sin(\theta_{zs})\approx\theta_{zs}$ and $\cos(\theta_{zs})\approx 1$ while other higher orders associated with θ_{zs} are neglected.

$$d_{y1}=\lambda_1\theta_{zs} \text{ and } d_{y2}=r_2\lambda_2\theta_{zs} \tag{6}$$

$$\theta_{zs} = \frac{\cos^2\alpha_2 r_2^3(A_1 f_{xs} + A_2 m_{zs})}{A_3 f_{xs} + A_4 f_{ys} + A_5 m_{zs} + A_6} \tag{7}$$

where A_1 through A_6 are the expressions of the independent geometric parameters and the loading position, as elaborated in Eq. (8).

$$A_1 = -\cos\alpha_2\sin\alpha_1\boldsymbol{h} - \cos\alpha_1\sin\alpha_2\boldsymbol{h} + \lambda_1\cos\alpha_1\sin\alpha_1\cos\alpha_2 + \lambda_1\cos^2\alpha_1\sin\alpha_2 \tag{8a}$$

$$A_2 = \cos\alpha_2\sin\alpha_1 + \cos\alpha_1\sin\alpha_2 \tag{8b}$$

$$\begin{aligned} A_3 = \frac{6}{5}(&-\cos\alpha_2\cos^2\alpha_1\sin\alpha_2\sin\alpha_1 r_2^2\lambda_1^2 \\ &+\cos^3\alpha_1\cos^2\alpha_2 r_2^2\lambda_1^2 - \cos^3\alpha_2 r_2^3\lambda_1 \\ &+\cos\alpha_1\cos^2\alpha_2\sin\alpha_2\sin\alpha_1 r_2^3\lambda_1^2 \\ &-\cos^2\alpha_2\sin\alpha_2\sin\alpha_1 r_2^3\boldsymbol{h}\lambda_1 - \cos^3\alpha_1 r_2^2\lambda_1^2 \\ &+\cos^3\alpha_2\cos\alpha_1\boldsymbol{h}r_2^3\lambda_1 + \lambda_1\cos^2\alpha_1\cos\alpha_2 r_2^3 \\ &-\cos^2\alpha_1\cos^2\alpha_2\boldsymbol{h}r_2^2\lambda_1 - \cos^3\alpha_2\cos^2\alpha_1 r_2^3\lambda_1^2 \\ &+\cos\alpha_2\cos\alpha_1\sin\alpha_2\sin\alpha_1\boldsymbol{h}r_2^2\lambda_1) \\ +\frac{2}{15}(&\cos^3\alpha_2 r_2^3 + 1.2\cos^3\alpha_2 r_2^3\lambda_1^2 - r_2^4\cos^2\alpha_2\cos\alpha_1) \end{aligned} \tag{8c}$$

$$\begin{aligned} A_4 = &\cos^3\alpha_2\sin\alpha_1 r_2^3\boldsymbol{h} - \cos\alpha_1\cos^3\alpha_2\sin\alpha_1 r_2^3\lambda_1 \\ &-\cos^2\alpha_1\cos^2\alpha_2\sin\alpha_2 r_2^3\lambda_1 \\ &+\frac{6}{5}(\cos^2\alpha_2\sin\alpha_2 r_2^3\lambda_1 + \lambda_1\cos\alpha_1\sin\alpha_1\cos\alpha_2 r_2^3 \\ &\quad -\cos^2\alpha_1\sin\alpha_1 r_2^2\lambda_1^2 - \cos^2\alpha_2\sin\alpha_2 r_2^3\lambda_1^2) \\ &-\frac{2}{15}(r_2^4\cos^2\alpha_2\sin\alpha_1 + \cos^2\alpha_2\sin\alpha_2 r_2^3 \\ &\quad +\cos\alpha_1\cos^2\alpha_2\sin\alpha_2 r_2^3\boldsymbol{h}) \end{aligned} \tag{8d}$$

$$\begin{aligned} A_5 = \frac{6}{5}(&\cos^2\alpha_2\sin\alpha_2\sin\alpha_1 r_2^3\lambda_1 - \cos^3\alpha_2\cos\alpha_1 r_2^3\lambda_1 \\ &+\cos^2\alpha_2\cos^2\alpha_1 r_2^2\lambda_1 - \cos\alpha_2\cos\alpha_1\sin\alpha_2\sin\alpha_1 r_2^2\lambda_1) \end{aligned} \tag{8e}$$

$$\begin{aligned} A_6 = 4(&r_2^2\cos^2\alpha_2\sin\alpha_2\cos\alpha_1 + \cos^3\alpha_2\sin\alpha_1 r_2^3 \\ &+\cos\alpha_1\cos^2\alpha_2\sin\alpha_2 r_2^3 + r_2^2\cos^3\alpha_2\sin\alpha_1) \\ +12(&\sin\alpha_1\cos^2\alpha_1\cos\alpha_2\lambda_1^2 - \cos\alpha_1\cos^2\alpha_2\sin\alpha_2 r_2^3\lambda_1 \\ &+\cos^3\alpha_2\sin\alpha_1 r_2^3\lambda_1^2 + \cos\alpha_1\cos^2\alpha_2\sin\alpha_2 r_2^3\lambda_1^2 \\ &-\lambda_1\cos^2\alpha_1\sin\alpha_2\cos\alpha_2 r_2 - \lambda_1\cos\alpha_1\sin\alpha_1\cos^2\alpha_2 r_2 \\ &+\cos^3\alpha_1\sin\alpha_2\lambda_1^2 - \cos^3\alpha_2\sin\alpha_1 r_2^3\lambda_1) \end{aligned} \tag{8f}$$

An FEA model of an IG-CSP is built in COMSOL 5.0. We assume the sheets are elastic and the motion stage is rigid. The maximum meshing size of the sheets is 0.814 (mm). The material is Aluminum: Young's modulus E=69×10^9 (Pa); Poisson's ratio v=0.33 and density is 2700 (kg/m^3). Let us consider an example to evaluate the accuracy of the analytical and closed-form models of the IG-CSP. We fix L_1, L_2, U, T, λ_1, α_1, and α_2 at 50 (mm), 30 (mm), 5 (mm), 0.5 (mm), 0.5, π/4, and π/6. A series of rotations range from 0 to 0.3 (rad) with a 0.02 (rad) step are prescribed on the rotational center of the IG-CSP. The results for the analytical, FEA, and the closed-formed models are illustrated in Fig. 5. When −0.3 (rad) < θ_{zs} < 0.3 (rad), the maximum error between analytical and FEA models is less than 5%; when −0.1 (rad) < θ_{zs} < 0.1 (rad), the maximum errors between the analytical and FEA models, closed-form and FEA models are less than 1.5% and 5%, respectively.

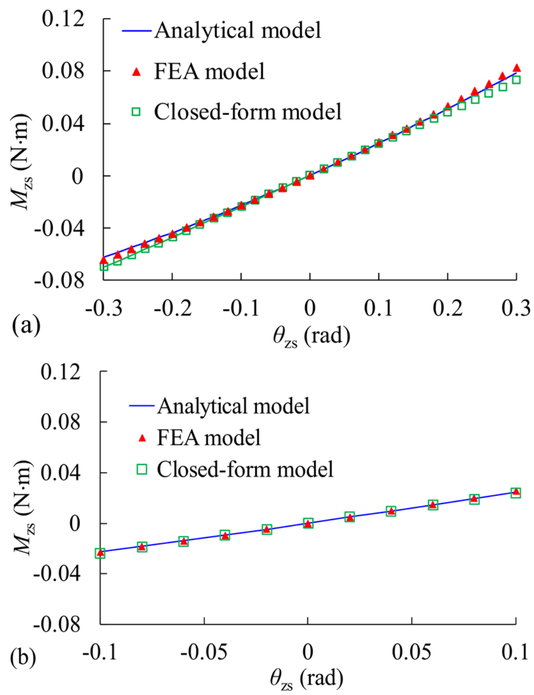

FIGURE 5: Comparisons of rotations for the analytical, closed-form and FEA models: (a)−0.3(rad)<θ_{zs}<0.3(rad), and (b)−0.1(rad)<θ_{zs} <0.1(rad).

2.2 The center shift model

D_x and D_y denote the normalized center shift along the X-axis and Y-axis, respectively. The normalized center shift based on the point S_1 can be derived as Eq. (9).

$$D_x = d_{x1}\sin\alpha_1 + d_{y1}\cos\alpha_1 - \lambda_1\sin(\alpha_1+\theta_{zs}) + \lambda_1\sin\alpha_1 \quad (9a)$$
$$D_y = -d_{x1}\cos\alpha_1 + d_{y1}\sin\alpha_1 - \lambda_1\cos\alpha_1 + \lambda_1\cos(\alpha_1+\theta_{zs}) \quad (9b)$$

Similarly, the center shift based on the point S_2 can also be derived as Eq. (10).

$$D_x = -d_{x2}\sin\alpha_2 + d_{y2}\cos\alpha_2 - \lambda_2 r_2\sin\alpha_2 + \lambda_2 r_2\sin(\alpha_2-\theta_{zs}) \quad (10a)$$
$$D_y = -d_{x2}\cos\alpha_2 - d_{y2}\sin\alpha_2 + \lambda_2 r_2\cos(\alpha_2-\theta_{zs}) - \lambda_2 r_2\cos\alpha_2 \quad (10b)$$

From Section 2.1, we have the outputs of the motion stage with given loading conditions and substituting these results into Eqs. (3) - (4) to obtain d_{xi} and d_{yi} (i=1 or 2). Then D_x and D_y are solved from Eqs. (9) or (10). We use the same example in Section 2.1 to verify the accuracy of the center shift, the comparison of center shift between the analytical and FEA models are shown in Fig. 6. The maximum errors of D_x and D_y are 1.7% and 5.2%, respectively.

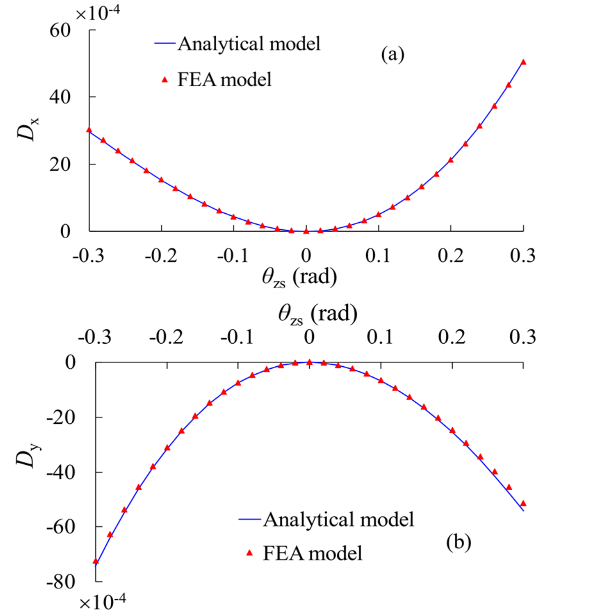

FIGURE 6: The comparison of the center shift between the analytical and FEA models: (a) D_x, And (b) D_y.

3. THE NONLINEAR ANALYSIS OF THE IS-CSP

In this section, the closed-form load-rotation relations of an IS-CSP and a NIS-CSP are derived, respectively. Then we analyze the effects of the geometric parameters, loading positions, and axial forces on the rotational stiffness of the IS-CSP. The load-dependent effects of an IS-CSP and a NIS-CSP are compared.

3.1 Load-rotation relation

The closed-form load-rotation relation of the IS-CSP is expressed as Eq. (11) by substituting r_2=1, $\alpha_1=\alpha_2=\alpha$, $\lambda_1=\lambda_2=\lambda$, into Eq. (7). λ, α and $\boldsymbol{h}$ are the independent parameters of the IS-CSP.

$$\theta_{zs} = \frac{15\cos\alpha(\cos\alpha f_{xs}\lambda - f_{xs}\boldsymbol{h} + m_{zs})}{(-18\lambda^2+18\lambda-15\lambda\cos^2\alpha+15\boldsymbol{h}\cos\alpha-2)f_{ys}+120\cos\alpha(3\lambda^2-3\lambda+1)} \quad (11)$$

In addition, the description of the NIS-CSP is shown in Fig. 7. The analytical model of a NIS-CSP is derived as below. Similar to the derivation in Section 2.1, we use $\mathbf{S}_{ni}$ to replace $\mathbf{S}_i$, $\mathbf{R}_{zni}$ to replace $\mathbf{R}_{zi}$ (i=1 or 2). S_{ni} denotes the free ends of the sheets in a NIS-CSP. $\mathbf{S}_{ni}$ denotes the coordinates of the point S_{ni} relative to the global coordinate system after only the rotation of the motion stage. $\mathbf{S}_{n1}=[-\lambda\sin(\alpha),-\boldsymbol{h},0]^T$, and $\mathbf{S}_{n2}=[\lambda\sin(\alpha),-\boldsymbol{h},0]^T$. $\mathbf{R}_{zni}$ denotes the rotational matrix about the Z-axis, $\mathbf{R}_{zni}=\begin{bmatrix}\cos\delta_i & -\sin\delta_i & 0\\ \sin\delta_i & \cos\delta_i & 0\\ 0 & 0 & 1\end{bmatrix}$. $\delta_1=-\pi/2-\alpha$ and $\delta_2=-\pi/2+\alpha$. The closed-form load-rotation relation of the NIS-CSP is expressed as Eq. (12),

$$\theta_{zs} = \frac{15\cos\alpha(-\cos\alpha f_{xs}\lambda - f_{xs}\boldsymbol{h} + m_{zs})}{(18\lambda^2-18\lambda+15\lambda\cos^2\alpha+15\boldsymbol{h}\cos\alpha+2)f_{ys}+120\cos\alpha(3\lambda^2-3\lambda+1)} \quad (12)$$

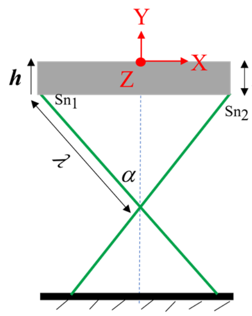

FIGURE 7: The description of a NIS-CSP.

3.2 Load-dependent effects

K_{zm} denotes the rotational stiffness due to the moment m_{zs} of an IS-CSP, which is expressed as Eq. (13) by rearranging Eq. (11). The rotational stiffness due to the bending force f_{xs} can be discussed in a similar way.

$$K_{zm} = A_m f_{ys} + 8(3\lambda^2 - 3\lambda + 1) \tag{13}$$

where $A_m = -2(9\lambda^2 - 9\lambda + 1)/(15\cos\alpha) - \lambda\cos\alpha + \boldsymbol{h} = A_{mgeo} + \boldsymbol{h}$. A_{mgeo} denotes the value of A_m due to the geometric parameters. $\boldsymbol{h}$ denotes the value of A_m due to the loading positions.

A_m is an expression of the independent geometric parameters (beam load-dependent effects) and loading positions (structure load-dependent effects). If $A_m = 0$, $A_m f_{ys} = 0$, f_{ys} has less effect on K_{zm} when a compressive axial force ($f_{ys} < 0$) acts on the IS-CSP. Meanwhile if $A_m > 0$, $A_m f_{ys} < 0$, K_{zm} decreases with f_{ys}, and vice versa. To analyze the effect of f_{ys} on K_{zm}, it is necessary to analyze the signs of A_m when λ, α, and $\boldsymbol{h}$ take different values.

A_m only relates to the geometric parameters, i.e. $A_m = A_{mgeo}$, when $\boldsymbol{h}$ is equal to 0. A_{mgeo} of an IS-CSP and a NIS-CSP are shown in Fig. 8, when λ and α range from 0 to 1 and 0 to $\pi/2$, respectively. When the geometric parameters of the IS-CSP are in the B region, $A_{mgeo} > 0$, the IS-CSP can be regarded as a non-inversed compliant sheet as K_{zm} decreases with a compressive f_{ys}. When the geometric parameters of the IS-CSP are in the C region, $A_{mgeo} < 0$, the IS-CSP can be regarded as an inversed compliant sheet. We can draw similar conclusions for a NIS-CSP operating in the D and E regions. In this way, if the geometric parameters are specifically given, A_{mgeo} can be determined from Fig. 8.

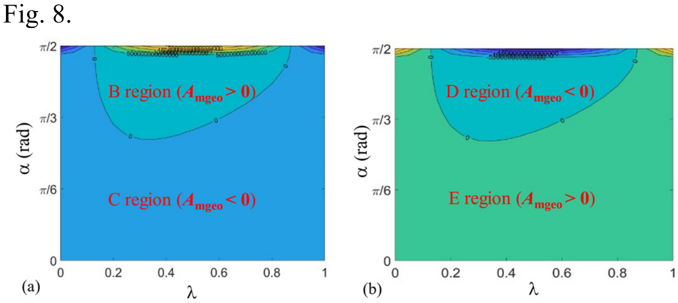

FIGURE 8: The effects of λ and α on A_{mgeo} of (a) an IS-CSP, and (b) a NIS-CSP.

On the other hand, the sign of A_m depends on the dominant position of A_{mgeo} and $\boldsymbol{h}$ as $A_m = A_{mgeo} + \boldsymbol{h}$. When λ and α are specifically given in the C region, A_{mgeo} is determined and less than 0, and K_{zm} increases with a compressive f_{ys} for the beam load-dependent effects ($A_{mgeo} f_{ys} > 0$). Under this condition, we analyze the structure load-dependent effects in C region. y_j (j=1, 2,…,or 7) denotes loading positions along the Y-axis as shown in Table 1 and Fig. 9(a). When the loading positions move from y_1 to y_6, $A_m = A_{mgeo} + h$, and K_{zm} decreases with a compressive f_{ys} for the structure load-dependent effects ($hf_{ys} < 0$). If $h > -A_{mgeo}$, i.e., $A_m > 0$, the structure load-dependent effects dominate K_{zm}. If $h < -A_{mgeo}$, i.e., $A_m < 0$, the beam load-dependent effects dominate K_{zm}. If $h = -A_{mgeo}$, i.e., $A_m = 0$, the equilibrium between structure and beam load-dependent effects is balanced, so when λ and α are specified, the load-dependent effects can be reduced significantly by regulating the loading positions. When the loading positions move from y_6 to y_7, $A_m = A_{mgeo} - h$, and A_m is always less than 0. K_{zm} increases with a compressive f_{ys} for both the beam and structure load-dependent effects. The equilibrium of beam and structure load-dependent effects in other regions can be analyzed similarly.

Moreover, if the loading position fixes at y_6, the region where $A_m < 0$ for an IS-CSP is increased. When the compressive axial forces ($f_{ys} < 0$) act on the IS-CSP, the region where $A_m f_{ys} > 0$ is increased, which means that the possibility of increasing K_{zm} rises. When the IS-CSP and NIS-CSP share the same λ, α, and $\boldsymbol{h}$, the absolute values of A_m are equal and the signs of A_m are opposite.

The effects of y_j (j=1, 2,…,or 7) on A_m of an IS-CSP are shown in Fig. 9(b) and Fig. 10. $\lambda = 1/2 \pm \sqrt{5}/6$ are two roots of $9\lambda^2 - 9\lambda + 1 = 0$ (Eq. (13)). In Fig. 9(b), when the loading positions range from y_1 to y_7, the curves representing $A_m = 0$ are enclosed gradually following the arrows' direction. The possibility of the geometric parameters are on the curve representing $A_m = 0$ can be increased. When the axial forces act on the rotational center (y_4) and λ is $1/2 - \sqrt{5}/6$ or $1/2 + \sqrt{5}/6$, A_m is equal to 0 without depending on α. In Fig. 10, when the loading positions range from y_1 to y_7, the region where $A_m < 0$ is increased. If h of y_1 is large enough, A_m is always greater than 0, which means that K_{zm} decreases with a compressive f_{ys}. Similarly, if h of y_7 is large enough, A_m is always smaller than 0, which means K_{zm} increases with f_{ys}. When $\boldsymbol{h}$ is specified, the load-dependent effects can be reduced significantly by taking any geometric parameters on the curve representing $A_m = 0$.

TABLE 1: The examples of loading locations y_j (j=1,2…or, 7), and Δ_1=20(mm)/L, Δ_2=10(mm)/L.

y_j	1	2	3	4	5	6	7
h	$y_2+\Delta_1$	$\cos\alpha$	$0.5(y_2+y_4)$	$\lambda\cos\alpha$	$0.5(y_4+y_6)$	0	$y_6+\Delta_2$
$\boldsymbol{h}$	h						$-h$

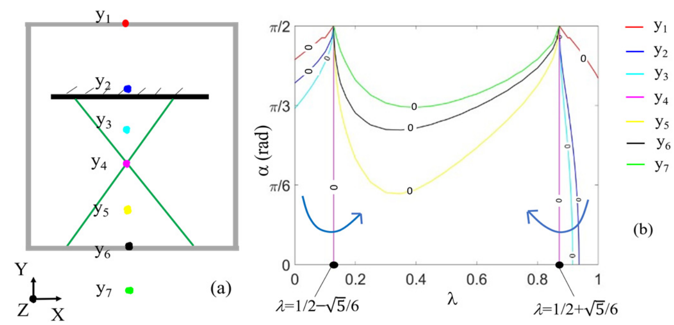

FIGURE 9: The effects of the loading positions on A_m of an IS-CSP: (a) the loading positions, (b) the curves representing A_m=0.

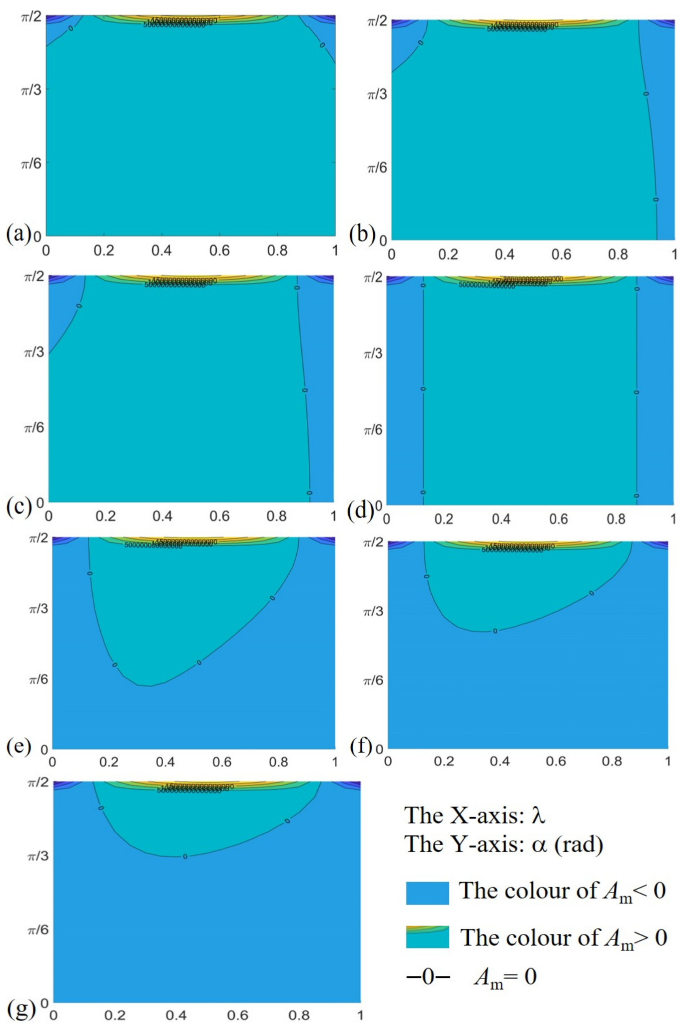

FIGURE 10: The effects of the loading positions on A_m of an IS-CSP: (a) y_1, (b) y_2, (c) y_3, (d) y_4, (e) y_5, (f) y_6, and (g) y_7.

To verify K_{zm} varying with the sign of A_m when f_{ys}<0, we take four cases of IS-CSPs to compare K_{zm} between the analytical and the FEA models. Table 2 lists the independent parameters of A_m (λ, α, h, $\boldsymbol{h}$), the signs of A_m, and the predictions of the load-dependent effects. The geometric parameters (λ, α) of Cases 1 and 2 are the same while the loading positions ($\boldsymbol{h}$) of Cases 1 and 2 are y_4 (the rotational center) and y_6, respectively. In Cases 3 and 4, the load-dependent effects of Case 2 can be reduced by regulating the loading position or the geometric parameters, respectively. When L is constant at 30(mm), θ_{zs} ranges from−0.1 (rad) to 0.1 (rad), K_{zm} for the four cases are shown in Fig. 11. The load-dependent effects of the predictions, analytical model, and FEA model are consistent. The maximum error of K_{zm} between the analytical and FEA models is 1.2%.

TABLE 2: Parameters of IS-CSPs ('↓, ↑, or c' denote that 'K_{zm} decreases, increases, or remains constant with f_{ys}', respectively).

Cases	λ	α	h	$\boldsymbol{h}$	A_m	K_{zm}
1			$\lambda\cos\alpha$	$\lambda\cos\alpha$	>0	↓
2		π/6	0	0	<0	↑
3	0.5		$\lvert A_{mgeo}\rvert$	$-A_{mgeo}$	0	c
4		54.735 π /180	0	0	0	c

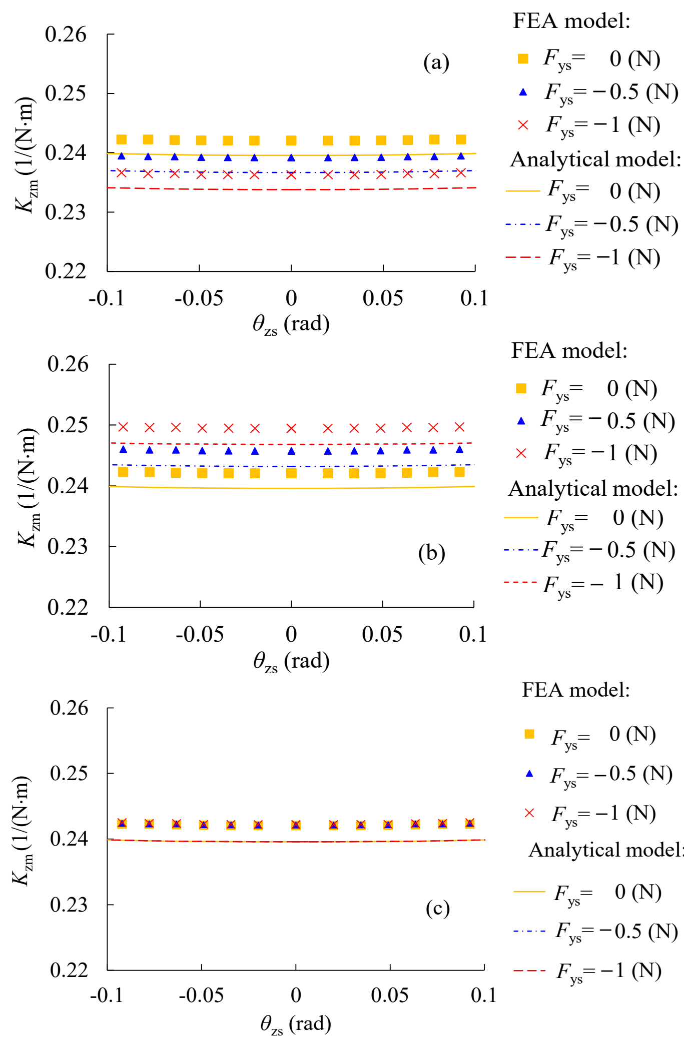

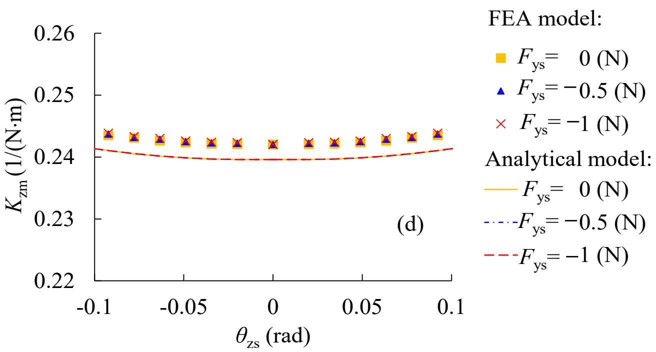

FIGURE 11: K_{zm} of: (a) case 1, (b) case 2, (c) case 3, and (d) case 4.

3.3 The closed-form model of the center shift

We derive the closed-form center shift of an IS-CSP referring to the method that Zhao et al. [9] have introduced.

D_x is derived as Eq. (14) for any values of λ. When λ is smaller than 0.5, the closed-form D_y can be directly derived from Eq. (6) as shown in Eq. (15), because the accuracy of Eq. (6) is highly acceptable. When λ is greater than 0.5, an accurate D_y with a more complex form is shown in Eq. (16) (derivation details can be seen in Ref.[9]), as the accuracy of Eq. (6) is compromised slightly. Besides, we do not discuss the center shift for the bending force f_{xs}, and assume f_{xs} is equal to 0 in this section.

$$
\begin{aligned}
D_x =& \frac{-(12\lambda-1)(9\lambda^2-9\lambda+1)\theta_{zs}^{\ 3}}{150\cos\alpha} \\
&+\frac{\left[12(-2\lambda+1)\cos\alpha\,\theta_{zs}\right]\left[\frac{1}{6300}(9\lambda^2-9\lambda+11)\theta_{zs}^{\ 2}+\frac{t^2}{12}\right]}{2\sin^2\alpha} \\
&+\frac{\left[\frac{1}{10}(12\lambda-1)f_{ys}\theta_{zs}\right]\left[\frac{1}{6300}(9\lambda^2-9\lambda+11)\theta_{zs}^{\ 2}+\frac{t^2}{12}\right]}{2\sin^2\alpha}
\end{aligned}
\tag{14}
$$

$$
\begin{aligned}
D_y =& \frac{1}{-15\cos\alpha}(-9\lambda^2+9\lambda-1)\theta_{zs}^{\ 2} \\
&+\frac{f_{ys}\left[\frac{1}{6300}(9\lambda^2-9\lambda+11)\theta_{zs}^{\ 2}+\frac{t^2}{12}\right]}{2\cos^2\alpha} \\
&-\frac{\theta_{zs}^{\ 4}}{3000\cos\alpha}(2592\lambda^4-3024\lambda^3+1338\lambda^2-241\lambda+2)
\end{aligned}
\tag{15}
$$

$$
\begin{aligned}
D_y =& \frac{1}{-15\cos\alpha}(-9\lambda^2+9\lambda-1)\theta_{zs}^{\ 2} \\
&+\frac{f_{ys}\left[\frac{1}{6300}(9\lambda^2-9\lambda+11)\theta_{zs}^{\ 2}+\frac{t^2}{12}\right]\left[\frac{11-12\lambda}{20}\left(\frac{1}{\cos^2\alpha}-\frac{1}{\sin^2\alpha}\right)\theta_{zs}^{\ 2}+\frac{1}{2}\left(\frac{1}{\cos^2\alpha}+\frac{\theta_{zs}^{\ 2}}{\sin^2\alpha}\right)\right]}{2\cos^2\alpha} \\
&-\frac{\theta_{zs}^{\ 4}}{\cos\alpha}\left[\frac{(2592\lambda^4-3024\lambda^3+1338\lambda^2-241\lambda+2)}{3000}-\frac{\cot^2\alpha(1-2\lambda)}{1050}(9\lambda^2-9\lambda+11)\right]
\end{aligned}
\tag{16}
$$

We use an example to evaluate the center shift between the closed-form and FEA models of an IS-CSP. L, U, T, α and λ are constant at 30 (mm), 5 (mm), 0.5 (mm), $\pi/6$, and 0.5 respectively. A series of prescribed rotations, ranging from −0.1 (rad) to 0.1 (rad) and F_{ys}=0 (N), act on the rotational centre of the IS-CSP. In Fig. 12, the maximum errors of D_x and D_y between closed-form and FEA models are 1.77% and 1.85%, respectively.

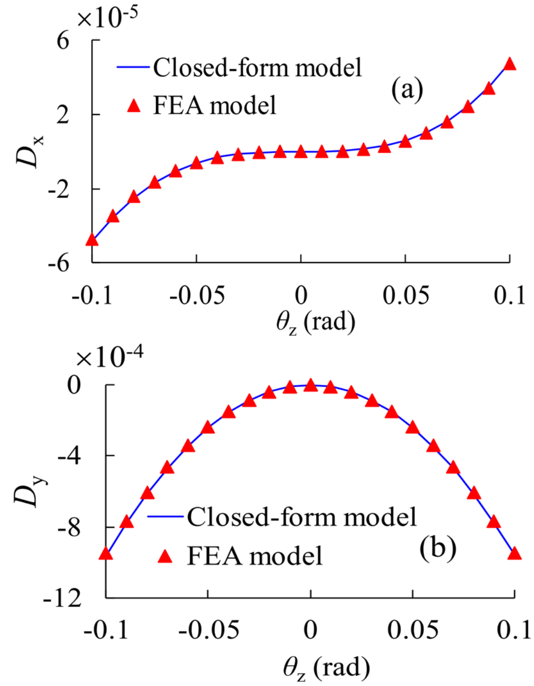

FIGURE 12: The center shift of the closed-form and FEA models: (a) D_x, and (b) D_y.

Comparing the coefficients of $9\lambda^2-9\lambda+1$ and f_{ys} in Eqs. (14) -(16), $9\lambda^2-9\lambda+1$ is a dominant item for both D_x and D_y. When $9\lambda^2-9\lambda+1=0$, D_x and D_y decrease significantly, and the axial force has less effect on D_x but a more significant effect on D_y as illustrated in Figs. 13(a) and (b). Zhao et al. reached the same conclusions in their research [9].

When $9\lambda^2-9\lambda+1\neq0$, the axial force does not influence both D_x and D_y significantly, and it is worth minimizing D_y because D_y is approximately ten times larger than D_x. For example, when λ is 0.4 or 0.7, the results of the center shift are shown in Figs. 13(c) - (f). We compare the center shifts between an IS-CSP and a NIS-CSP. The geometric parameters of Fig. 12 are used for both an IS-CSP and a NIS-CSP. A series of prescribed rotations, ranging from −0.1 (rad) to 0.1 (rad) and an axial force of −1 (N), act on their rotational centers. Their center shifts are compared as shown in Fig. 14. Note that Figs. 14(a) and (b) share the same legend. When an IS-CSP and a NIS-CSP are under a same rotational angle, the absolute values of their center shifts are close, and directions are opposite.

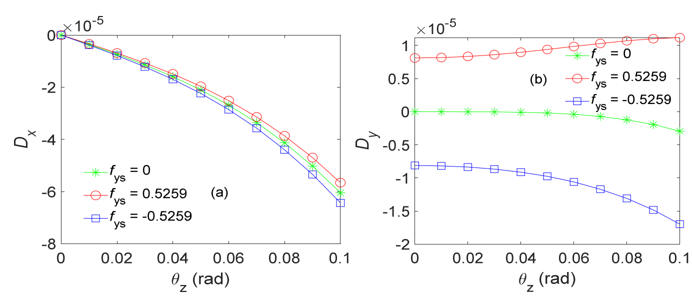

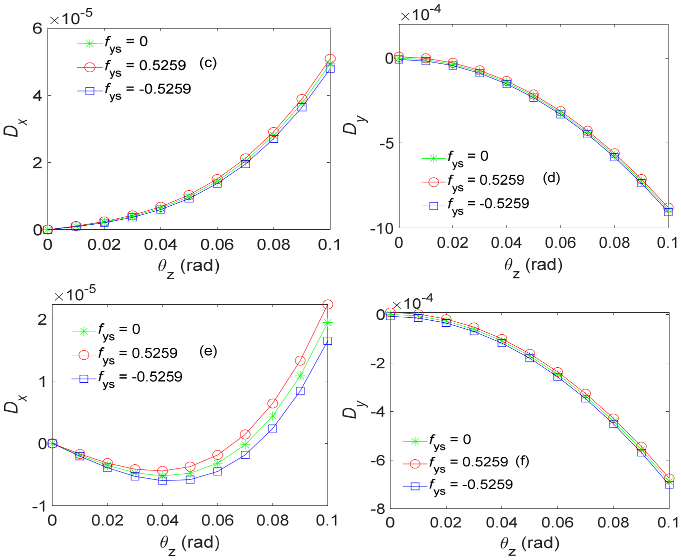

FIGURE 13: The effects of f_{ys} on D_x and D_y of the closed-form models: (a) D_x when λ is $1/2+\sqrt{5}/6$, (b) D_y when λ is $1/2+\sqrt{5}/6$, (c) D_x when λ is 0.4, (d) D_y when λ is 0.4, (e) D_x when λ is 0.7, and (f) D_y when λ is 0.7.

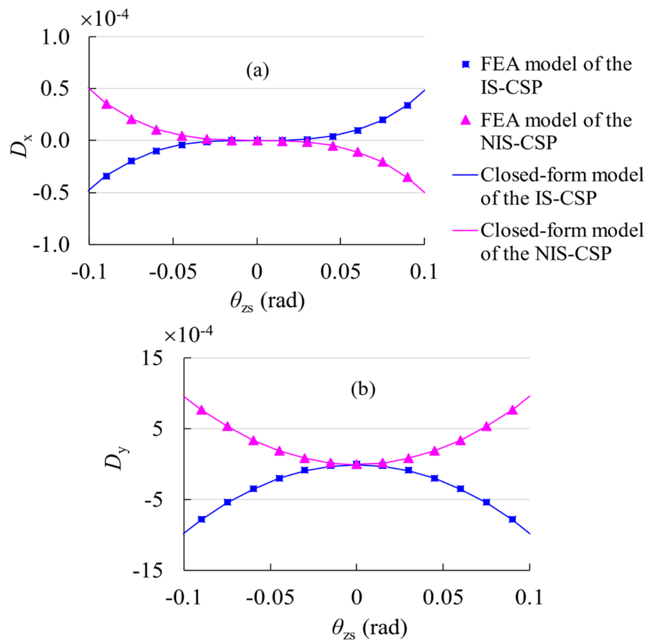

FIGURE 14: The center-shift comparison between an IS-CSP and a NIS-CSP: (a) D_x, and (b) D_y.

4. DESIGN OF THE COMPOUND S-CSP

In this section, we present two novel compound S-CSPs, including a parallel design and a serial design, and each design consists of an IS-CSP and a NIS-CSP, whose geometric parameters are the same correspondingly. They are regarded as two basic units, and each design can be modelled as the two basic units connected in a parallel (or serial) arrangement. The analytical models of an IS-CSP and a NIS-CSP are referred to Sections 2.1 and 3.1, respectively. O_1-$X_1Y_1Z_1$ and O_2-$X_2Y_2Z_2$ denote the local coordinate systems of the IS-CSP and NIS-CSP, respectively. O_s-$X_sY_sZ_s$ denotes the global coordinate system of each design. Their origins locate at the rotation center, so the displacements with regard to the global coordinate system are the center shift of each design.

We evaluate the characteristics by the analytical and FEA models, and fix L, U, T, α and λ for each design, which are 30 (mm), 5 (mm), 0.5 (mm), $\pi/6$, and 0.5, respectively.

4.1 A parallel design: Design I

Inspired by Ref. [24] and Sections 3.2, the description of design I is shown in Fig. 15(a). The rotational stiffness of design I can be insensitive to axial forces when an applied moment is constant. The additional benefit of this design lies in the minimized center shift. The analytical model of design I is derived as follows. The compatibility conditions and load-equilibrium equations are illustrated in Eqs. (17) and Eq. (18). d_{xsDI}, d_{ysDI}, and θ_{zsDI} are solved with given f_{xsDI}, f_{ysDI}, and m_{zsDI}.

$$\begin{gathered} d_{xsDI}=d_{xs1}=d_{xs2} \\ d_{ysDI}=d_{ys1}=d_{ys2} \\ \theta_{zsDI}=\theta_{zs1}=\theta_{zs2} \end{gathered} \tag{17}$$

$$\begin{gathered} f_{xsDI}=f_{xs1}+d_{xs2} \\ f_{ysDI}=f_{ys1}+f_{ys2} \\ m_{zsDI}=m_{zs1}+m_{zs2} \end{gathered} \tag{18}$$

where, f_{xsDI}, f_{ysDI}, m_{zsDI}, f_{xs1}, f_{ys1}, m_{zs1}, f_{xs2}, f_{ys2}, and m_{zs2} denote the normalized loads of the design I, IS-CSP, and NIS-CSP, respectively, as shown in Figs. 15(b) and (c). d_{xsDI}, d_{ysDI}, θ_{zsDI}, d_{xs1}, d_{ys1}, θ_{zs1}, d_{xs2}, d_{ys2} and θ_{zs2} denote the normalized displacements and rotation angles correspondingly.

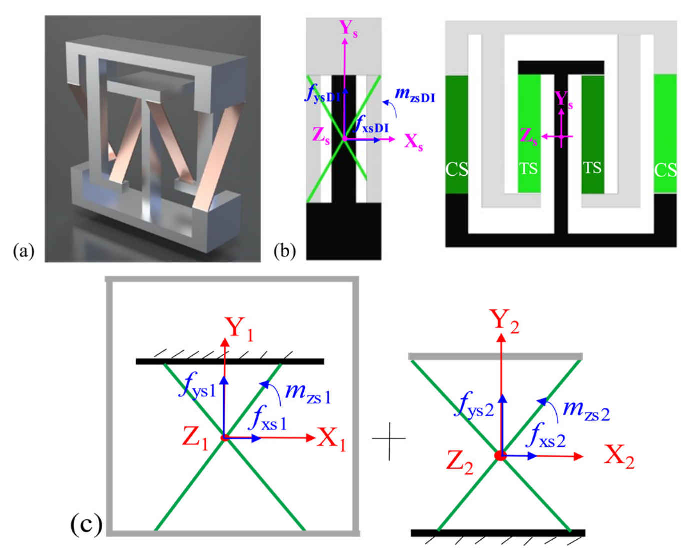

FIGURE 15: Descriptions of the design I: (a) a 3D model, (b) the global coordinate system, and (c) the local coordinate systems ('CS' denotes a compressive sheet, 'TS' denotes a tensile sheet).

Similar to the discussion in Section 3.2, the load-dependent effects of design I depend on A_m of design I (denoted by A_{mDI} in this section). A_{mDI} approximates the result of adding each CSP's

A_m when the two CSPs are arranged in parallel to form design I, i.e., $A_{mDI} \approx$ 'A_{mgeo}+$\boldsymbol{h}$ of IS-CSP' + 'A_{mgeo}+$\boldsymbol{h}$ of NIS-CSP'. Because the centre shifts of two individual CSPs move in the opposite direction, and the actual rotational stiffness of design I (denoted by K_{zmDI}) is larger than the simple stiffness addition of two individual CSPs (i.e., load-stiffening effect). 'A_{mgeo}+$\boldsymbol{h}$ of IS-CSP' refers to Eq. (13), and 'A_{mgeo}+$\boldsymbol{h}$ of NIS-CSP' can be derived from Eq. (12). A_{mgeo} of IS-CSP is always counteracted by that of the NIS-CSP when they have the same geometric parameters. Therefore, the load-dependent effects of design I due to geometric parameters almost disappear. However, $\boldsymbol{h}$ of the two CSPs are not always counteracted with each other. The load-dependent effects of design I due to loading positions are analyzed as follows.

The rotations of design I obtained from the analytical and FEA models under different loading positions and axial forces are shown in Fig. 16. $\boldsymbol{L}_{cy}$ denotes a directional distance between the rotational center and the loading position, where $\boldsymbol{L}_{cy}>0$ and $\boldsymbol{L}_{cy}<0$ mean that the loading positions are above and below the rotational center, respectively. $\boldsymbol{L}_{cy}$ ranges from 30 (mm) to −30 (mm) with a −10 (mm) step. F_{ysDI} ranges from −4 (N) to 4 (N) with a 0.5 (N) step acting on the loading positions, and M_{zsDI} is kept unchanged at 0.04 (N·m). The maximum error between analytical and FEA models is 2.5%.

When $|\boldsymbol{L}_{cy}|\leq 20$ (mm), the maximum error of θ_{zsDI} between $|F_{ysDI}|$ = 4 (N) and F_{ysDI}=0 is 5.0%. However, when $|\boldsymbol{L}_{cy}|$ = 30 (mm), the maximum error of θ_{zsDI} between $|F_{ysDI}|$=4 (N) and F_{ysDI}=0 is 7.7%. With the same M_{zsDI}, axial forces influence θ_{zsDI} slightly within a specified $|\boldsymbol{L}_{cy}|$ but they affect θ_{zsDI} significantly if $|\boldsymbol{L}_{cy}|$ is large enough.

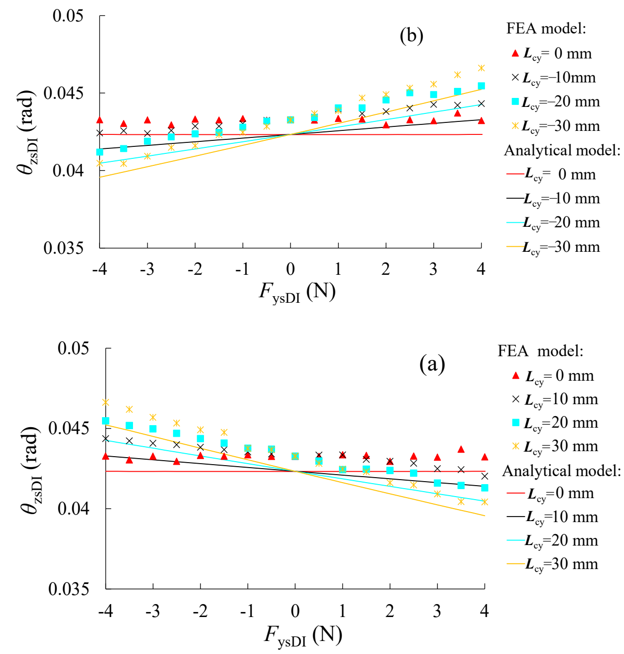

FIGURE 16: The effects of loading positions and axial forces on θ_{zsDI} with M_{zsDI} = 0.04 (N·m): (a) above the rotational center ($\boldsymbol{L}_{cy}>0$), and (b) below the rotational center ($\boldsymbol{L}_{cy}<0$).

We use A_{mDI} to explain how θ_{zsDI} varies with F_{ysDI} in Fig. 16. When $|\boldsymbol{L}_{cy}|$=0 or 20 (mm), A_{mDI}, and the predictions of K_{zmDI} and θ_{zsDI}, corresponding to different F_{ysDI}, are illustrated in Table 3. When the loading position is the rotational center (i.e., $\boldsymbol{L}_{cy}$=0), A_m of one CSP is counteracted by that of the other CSP, leading to $A_{mDI}\approx 0$. Therefore, K_{zmDI} and θ_{zsDI} remain constant with different F_{ysDI}. When L_{cy}=20 (mm), $A_{mDI}>0$, so K_{zmDI} decreases and θ_{zsDI} increases under a compressive F_{ysDI}. When L_{cy}=−20 (mm), K_{zmDI} and θ_{zsDI} can be similarly analyzed.

TABLE 3: Load-dependent results of design I when $|\boldsymbol{L}_{cy}|$=20 (mm) or 0 (mm). ('↓, ↑, or c' denote that 'K_{zm} of design I decreases, increases, or remains constant with F_{ysDI}', respectively. '+' denotes '$F_{ysDI}>0$', and '−' denotes '$F_{ysDI}<0$'.)

$\boldsymbol{L}_{cy}$ (mm)	CSP	A_{mgeo}	$\boldsymbol{h}$ of each CSP		A_m of each CSP	A_{mDI}	F_{ysDI}	K_{zmDI}	θ_{zsDI}
0	IS	−0.24	$\lambda\cos(\alpha)$=	0.43	0.19	0	−	c	c
	NIS	0.24	$-\lambda\cos(\alpha)$=	−0.43	−0.19		+	c	c
20	IS	−0.24	$\lambda\cos(\alpha)+\boldsymbol{L}_{cy}/L$=	1.10	0.86	1.33>0	−	↓	↑
	NIS	0.24	$-\lambda\cos(\alpha)+\boldsymbol{L}_{cy}/L$=	0.23	0.47		+	↑	↓
−20	IS	−0.24	$\lambda\cos(\alpha)+\boldsymbol{L}_{cy}/L$=	−0.23	−0.47	−1.33<0	−	↑	↓
	NIS	0.24	$-\lambda\cos(\alpha)+\boldsymbol{L}_{cy}/L$=	−1.10	−0.86		+	↓	↑

4.2 A serial design: Design II

Inspired by Section 3.3, design II has a small center shift as shown in Fig. 17(a), and the compatibility conditions and the load-equilibrium equations of the analytical model are illustrated in Eqs. (19) and (20), respectively. d_{xsDII}, d_{ysDII}, and θ_{zsDII} are solved with given f_{xsDII}, f_{ysDII}, and m_{zsDII}.

$$\begin{aligned} d_{xsDII} &= d_{xs2}+d_{xs1}\cos(\theta_{zs2})-d_{ys1}\sin(\theta_{zs2}) \\ d_{ysDII} &= d_{ys2}+d_{xs1}\sin(\theta_{zs2})+d_{ys1}\cos(\theta_{zs2}) \\ \theta_{zsDII} &= \theta_{zs1}+\theta_{zs2} \end{aligned} \tag{19}$$

$$\begin{aligned} f_{xsDII} &= f_{xs1}\cos(\theta_{zs2})-f_{ys1}\sin(\theta_{zs2}) \\ f_{ysDII} &= f_{xs1}\sin(\theta_{zs2})+f_{ys1}\cos(\theta_{zs2}) \\ f_{xs2} &= f_{xs1}\cos(\theta_{zs2})-f_{ys1}\sin(\theta_{zs2}) \\ f_{ys2} &= f_{xs1}\sin(\theta_{zs2})+f_{ys1}\cos(\theta_{zs2}) \\ m_{zsDII} &= m_{zs1}= m_{zs2} \end{aligned} \tag{20}$$

where, f_{xsDII}, f_{ysDII}, and m_{zsDII} denote the normalized loads of the design II as shown in Figs. 17(b) and (c). d_{xsDII}, d_{ysDII}, and θ_{zsDII} denote the normalized displacements and rotation angles correspondingly.

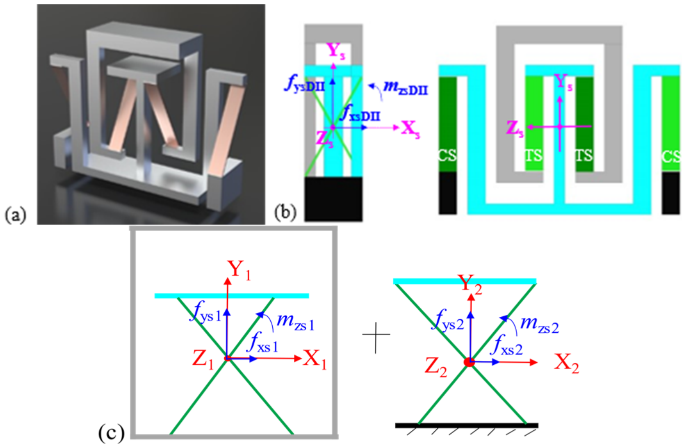

FIGURE 17: Descriptions of design II: (a) a 3D model, (b) the global coordinate system, and (c) the local coordinate systems.

When $F_{xsDII}=0$, $F_{ysDII}=-0.5$(N), M_{zsDII} ranges from 0.001 to 0.015 (N·m), the results between analytical and FEA models are shown in Fig. 18. The maximum errors of d_{xsDII}, d_{ysDII}, and θ_{zsDII} are 5.7%, 4.7%, and 1.67%, respectively. The center shift along the X-axis and Y-axis of the design II are reduced by 10 and 100 times, respectively, compared with those of an S-CSP (Fig. 14).

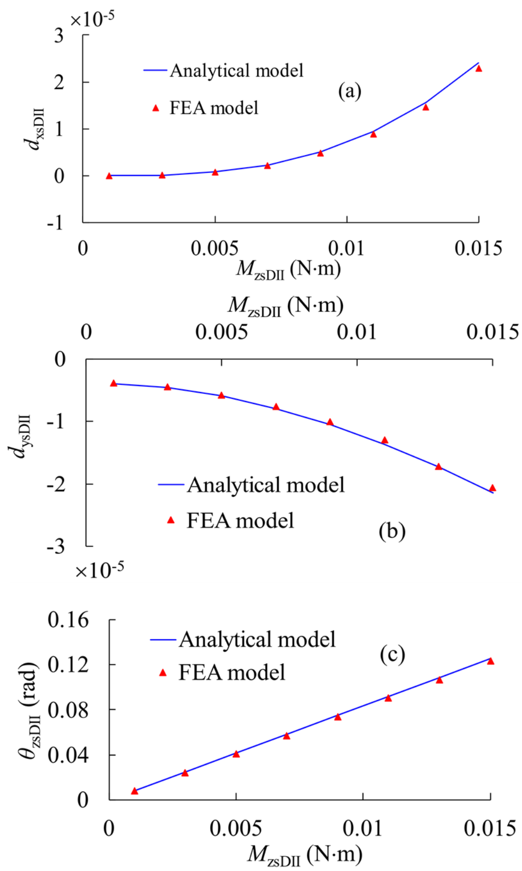

FIGURE 18: The results of analytical and FEA models of the design II with $F_{ysDII}=-0.5$(N): (a) d_{xsDII}, (b) d_{ysDII}, and (c) θ_{zsDII}.

Figure 19 illustrates the performance differences between designs I and II. When the rotational angle is fixed at 0.04 (rad) acting on the motion stage, the center shifts of the FEA models of design I and II are as follows: $d_{xsDI}=1.02\times10^{-17}$, $d_{ysDI}=-4.17\times10^{-18}$, $d_{xsDII}=7.60\times10^{-7}$, and $d_{ysDII}=1.52\times10^{-8}$. The magnitudes of the center shift of design I are much smaller than those of design II. However, when the moment is fixed, design II' rotational range is much larger than that of the design I. Design II is an ideal candidate for the application requiring the rotational ranges with a minimized center shift. On the other hand, the rotational stiffness of design I with any λ can be insensitive to axial loads, when M_{zsDI} is fixed. If the axial forces act on the rotational center ($\boldsymbol{L}_{cy}=0$), the loading positions and axial forces do not influence θ_{zsDI}. If the axial forces do not act on the rotational center, axial forces can influence θ_{zsDI} slightly within specified loading positions.

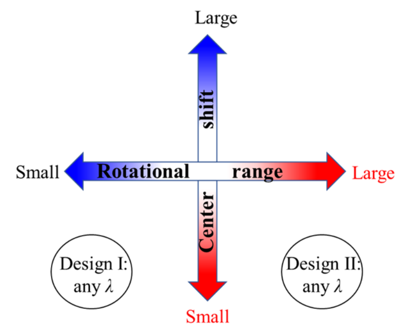

FIGURE 19: Center-shift and rotational-range comparisons between designs I and II.

5. CONCLUSIONS

The closed-form model of an IG-CSP based on BCM is derived, along with the closed-form load-rotation relation of the IS-CSP. We take the axial force (f_{ys}), geometric parameters, and the loading positions into consideration of the load-rotation relation of the S-CSP for analyzing the load-dependent effects.

The load-dependent effects include the beam load-dependent effects and the structure load-dependent effects. The rotational stiffness can increase, decrease, or remain constant with the axial forces (f_{ys}) depending on the equilibrium of the beam load-dependent effects and the structure load-dependent effects. The coefficient of f_{ys} of the S-CSP load-rotation relation is A_m, which is an expression of geometric parameters (λ, α) and the loading positions ($\boldsymbol{h}$). The load-dependent effects can be designed by regulating the positive or negative sign of $A_m f_{ys}$. In other words, the equilibrium between the structure and beam load-dependent effects can be controlled by regulating λ, α and $\boldsymbol{h}$. If an IS-CSP and a NIS-CSP are subjected to the same geometric parameters, axial loads, and loading positions, the absolute values of A_m are equal and the signs of A_m are opposite.

The closed-form center shift of the IS-CSP is derived and verified by analytical and FEA models. $9\lambda^2-9\lambda+1$ is a dominant term of the closed-form center shift solution. When $9\lambda^2-9\lambda+1$ is not equal to 0, the axial forces have less effect on D_x and D_y. When an IS-CSP and a NIS-CSP have the same geometric parameter (required $9\lambda^2 - 9\lambda+1\neq0$) and are subjected to the same loading conditions, their absolute values of the center shift are close and their directions are opposite correspondingly.

Based on the above nonlinear analysis, two compound S-CSPs are proposed. When the applied moment is constant, the loading positions and axial forces can slightly influence the rotational stiffness of design I. Compared with an S-CSP, design II enlarges the rotations and minimizes the center shift along the X-axis and Y-axis by 10 and 100 times, respectively. In the future, the load-dependent effects and the effects of the axial forces on the center shift of the IG-CSP will be discussed.

DECLARATION OF COMPETING INTEREST

The authors declare that they have no known competing financial interests or personal relationships that could have appeared to influence the work reported in this paper.

ACKNOWLEDGEMENTS

The authors would like to sincerely thank Xiuyun He for her help in producing the two rendered images. Alison O'Shea is also appreciated for her help in checking grammar of Chapter 3. Shiyao Li and Jiaxiang Zhu are both funded by the China Scholarship Council.

REFERENCES

[1] J. Dearden, C. Grames, J. Orr, B. D. Jensen, S. P. Magleby, and L. L. Howell, "Cylindrical cross-axis flexural pivots," *Precis. Eng.*, vol. 51, pp. 604–613, 2018.

[2] B. D. Jensen and L. L. Howell, "The modeling of cross-axis flexural pivots," *Mech. Mach. Theory*, vol. 37, no. 5, pp. 461–476, 2002.

[3] P. Bilancia, M. Baggetta, G. Berselli, L. Bruzzone, and P. Fanghella, "Design of a bio-inspired contact-aided compliant wrist," *Robot. Comput. Integr. Manuf.*, vol. 67, no. July 2020, p. 102028, 2021.

[4] V. Tielen and Y. Bellouard, "Three-dimensional glass monolithic micro-flexure fabricated by femtosecond laser exposure and chemical etching," *Micromachines*, vol. 5, no. 3, pp. 697–710, 2014.

[5] S. Bi, Y. Li, and H. Zhao, "Fatigue analysis and experiment of leaf-spring pivots for high precision flexural static balancing instruments," *Precis. Eng.*, vol. 55, no. June 2018, pp. 408–416, 2019.

[6] X. Pei, J. Yu, G. Zong, and S. Bi, "A family of butterfly flexural joints: Q-litf pivots," *J. Mech. Des. Trans. ASME*, vol. 134, no. 12, pp. 1–8, 2012.

[7] X. Pei, J. Yu, G. Zong, S. Bi, and Z. Yu, "Analysis of rotational precision for and isosceles-trapezoidal flexural pivot," *J. Mech. Des. Trans. ASME*, vol. 130, no. 5, pp. 1–9, 2008.

[8] A. E. Guérinot, S. P. Magleby, and L. L. Howell, "Preliminary design concepts for compliant mechanism prosthetic knee joints," in *Proceedings of the ASME Design Engineering Technical Conference*, 2004, vol. 2 B, pp. 1103–1111.

[9] H. Zhao and S. Bi, "Accuracy characteristics of the generalized cross-spring pivot," *Mech. Mach. Theory*, vol. 45, no. 10, pp. 1434–1448, 2010.

[10] S. Zelenika and F. De Bona, "Analytical and experimental characterisation of high-precision flexural pivots subjected to lateral loads," *Precis. Eng.*, vol. 26, no. 4, pp. 381–388, 2002.

[11] H. Zhao, D. Han, and S. Bi, "Modeling and Analysis of a Precise Multibeam Flexural Pivot," *J. Mech. Des. Trans. ASME*, vol. 139, no. 8, pp. 1–9, 2017.

[12] X. Pei, J. Yu, G. Zong, and S. Bi, "The stiffness model of leaf-type isosceles-trapezoidal flexural pivots," *J. Mech. Des. Trans. ASME*, vol. 130, no. 8, pp. 0823031–0823036, 2008.

[13] L. L. Howell, *Compliant mechanism*. Wiley, New York, 2001.

[14] G. Hao, X. Kong, and R. L. Reuben, "A nonlinear analysis of spatial compliant parallel modules: Multi-beam modules," *Mech. Mach. Theory*, vol. 46, no. 5, pp. 680–706, 2011.

[15] H. Zhao and S. Bi, "Stiffness and stress characteristics of the generalized cross-spring pivot," *Mech. Mach. Theory*, vol. 45, no. 3, pp. 378–391, 2010.

[16] H. Zhao, S. Bi, and J. Yu, "Nonlinear deformation behavior of a beam-based flexural pivot with monolithic arrangement," *Precis. Eng.*, vol. 35, no. 2, pp. 369–382, 2011.

[17] S. Bi, H. Zhao, and J. Yu, "Modeling of a cartwheel flexural pivot," *J. Mech. Des. Trans. ASME*, vol. 131, no. 6, pp. 0610101–0610109, 2009.

[18] A. Zhang, Y. Gou, and X. Yang, "Predicting Nonlinear Stiffness, Motion Range, and Load-Bearing Capability of Leaf-Type Isosceles-Trapezoidal Flexural Pivot Using Comprehensive Elliptic Integral Solution," *Math. Probl. Eng.*, vol. 2020, pp. 1–11, 2020.

[19] E. G. Merriam and L. L. Howell, "Non-dimensional approach for static balancing of rotational flexures," *Mech. Mach. Theory*, vol. 84, pp. 90–98, 2015.

[20] S. Awtar, "Synthesis and analysis of parallel Kinematic XY flexure mechanisms," *Massachusetts Inst. Technol. Dept Mech. Eng.*, vol. 126, no. December 2003, p. 109, 2004.

[21] K. Wu and G. Hao, "Design and nonlinear modeling of a novel planar compliant parallelogram mechanism with general tensural-compresural beams," *Mech. Mach. Theory*, vol. 152, pp. 1–23, 2020.

[22] K.M. Lee and J. Guo, "Kinematic and dynamic analysis of an anatomically based knee joint," *J. Biomech.*, vol. 43, no. 7, pp. 1231–1236, 2010.

[23] G. Hao and X. Kong, "A normalization-based approach to the mobility analysis of spatial compliant multi-beam modules," *Mech. Mach. Theory*, vol. 59, pp. 1–19, 2013.

[24] G. Hao, X. He, and S. Awtar, "Design and analytical model of a compact flexure mechanism for translational motion," *Mech. Mach. Theory*, vol. 142, p. 103593, 2019.